Supporting Information:Comparing Interfacial Cation Hydration at Catalytic Active Sites and Spectator Sites on Gold Electrodes: Understanding Structure Sensitive CO_2 Reduction Kinetics

Jaclyn A. Rebstock, Quansong Zhu, and L. Robert Baker*

Department of Chemistry and Biochemistry, The Ohio State University, Columbus, Ohio 43210, United States

E-mail: baker.2364@osu.edu

Phone: +1 (614) - 292 - 2088

Contents

1. Sum frequency generation spectroscopy setup

The VSFG system has been described in detail previously;[1] however, we give a brief description of the system here. The VSFG system uses a femtosecond Ti:Sapphire regenerative amplifier (Spectra Physics-Solstice) that produces 90 fs pulses centered at 800 nm with an average power of 3.5 W and a 2 kHz repetition rate. Seventy percent of the output was used to pump an OPA (Topaz Prime) with non-collinear difference-frequency generation. The OPA produced a tunable, broadband infrared (IR) beam. To probe the CO stretch, the IR beam was centered at $\sim$2100 cm^{-1} with an energy of $\sim$5 μJ. The remaining thirty percent of the output beam was spectrally narrowed to $\sim$10 cm^{-1} using an air-spaced etalon. The narrowed visible beam had an energy of about 10 μJ and a 0.128 mm^2 beam area. The visible and IR beams were overlapped spatially onto the sample in a Kretschmann configuration at a 56° incident angle. The envelope of the non-resonant peak with complete temporal overlap of the visible and IR beams is given in Figure S1a. To collect CO spectra, the visible field was time delayed 730 fs relative to the IR field and the VSFG signal was integrated for 2 min. Figure S1b shows the non-resonant suppression by increasing the time delay of the visible field. The signal was integrated for 120 s to show that the non-resonant signal is fully suppressed under experimental conditions.

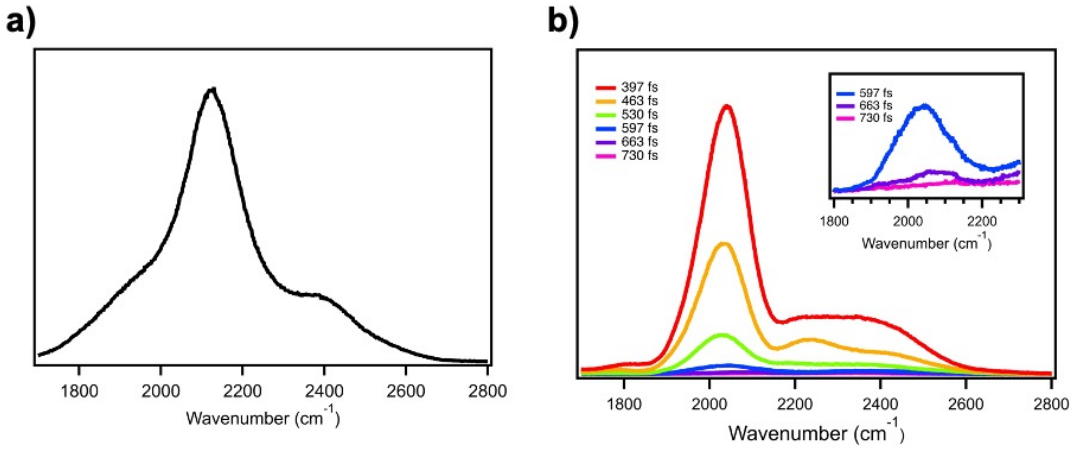

Figure S1: a) The non-resonant envelope of Au in air with complete overlap of the visible and IR beams under 1 s integration. b) The non-resonant envelope of Au in air as a response to the visible beam time delay under 120 s integration.

2. CO spectra measurement

VSFG measurements of CO were made with polycrystalline Au deposited on CaF_2 windows. 35 nm of Au was deposited by electron beam evaporation (Denton DV-502A E-Gun Evaporator). The CaF_2 windows were cleaned with basic Piranha (H_2O:H_2O_2:NH_4OH=5:1:1 Caution: Pirhana solutions are caustic and should be handled with extreme care) at 80 °C for one hour before the deposition. The Au electrode was then placed onto the homemade VSFG cell for spectroscopic measurement.[1,2] A Pt mesh was used as the counter electrode, while a leakless Ag/AgCl electrode (eDAQ ET072-1) was used as the reference electrode. To avoid Pt contamination on Au, a Nafion membrane (selectively exchanging protons) was employed to separate the cathodic and anodic compartments. The electrolytes were prepared by purging 0.05 M M_2CO_3 (M=Li(99.997%), Na(99.999%), K(99.995%), Rb(99.8%), Cs(99.995%), Sigma-Aldrich) with CO_2 for 10 minutes to convert M_2CO_3 to $MHCO_3$. Then it was purged with CO at 0.1 ft^3/h for 10 min to saturate the electrolyte with CO. CO was continuously purged during the measurements. For EDTA measurements, 3.4 μM of EDTA was added to the electrolyte while all other conditions were kept the same.

A BioLogic SP-150 potentiostat was used to control the applied potential. Potential steps from -0.1 V to -0.9 V vs. Ag/AgCl were applied to the Au electrode, staying at each potential step for 1 min before VSFG CO spectra were collected. The resulting CO spectra were fitted with a Lorentizan function to obtain the peak position.

To confirm that the peaks assigned as COAS and COSS are actual resonant modes and not the result of resonant/non-resonant interactions, we have measured the vibrational spectra in 0.1 M $NaHCO_3$ during CO purging at two different potentials while tuning the center of the IR wavelength with a fixed 730 fs time delay between IR and visible fields. In these spectra, the resonant peaks assigned as COSS (panel A) and COAS (panel B) do not shift as a function of the mid-IR center. Additionally, we measured the corresponding non-resonant signal also in 0.1 M $NaHCO_3$ during CO purging at 0 fs time delay between the visible and IR beams. Unlike the resonant signals, the non-resonant signal shifts as expected. Together

this data confirms that the measured frequency of COSS and COAS modes is not influenced by resonant/non-resonant interactions.

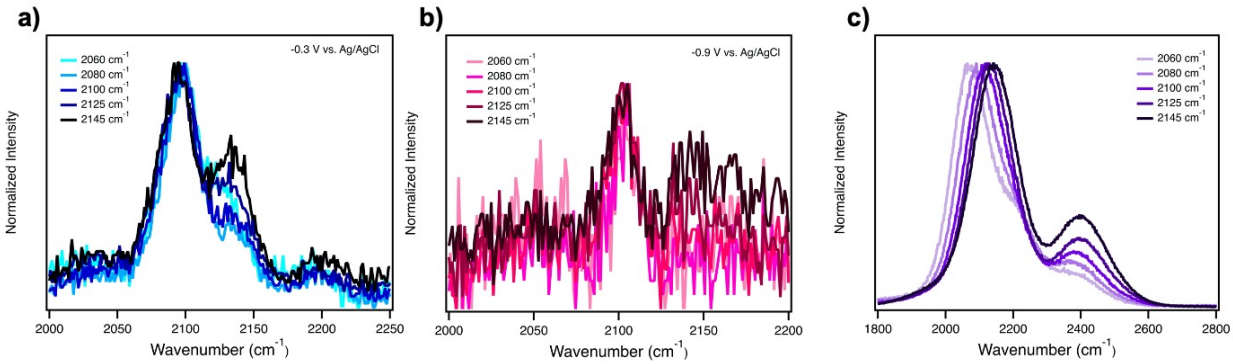

Figure S2: a) Normalized spectra of the COSS feature as a function of the mid-IR center in 0.1 M $NaHCO_3$ and a 730 fs time delay. b) Normalized spectra of the COAS feature as a function of the mid-IR center in 0.1 M $NaHCO_3$ and a 730 fs time delay. c) Normalized spectra of the non-resonant envelope as a function of the mid-IR center in 0.1 M $NaHCO_3$ and 0 fs time delay.

3. Kinetics Measurement

The kinetics measurement for the CO Faradaic efficiency of CO has been described elsewhere,[3] but we provide a summary here. The measurement was made on a 100 nm polycrystalline Au sample that was deposited on a microscope slide with a 20 nm Cr adhesion layer. The electrochemical H-cell was connected to an Agilent 7890B gas chromatograph through a custom headspace sampling system. Two compartments of the H-cell were separated by a Nafion membrane, which was activated in 10 % H_2SO_4 at 80 °C for 10 min before each experiment. A Ag/AgCl electrode was used as the reference electrode while a Pt thin film electrode was used as the counter electrode. The electrolyte was purged with CO_2 for 15 min at a rate of 0.35 L/min to convert Na_2CO_3 into $NaHCO_3$ at the beginning of the measurement. During the measurement, a constant potential, i.e. -1.2 V vs. Ag/AgCl, was applied to the Cr/Au working electrode by a Biologic SP-50 potentiostat, while simultaneously sampling from the headspace and injecting the sample gas into the GC every 20 min. The process was repeated three times for both unpurified and purified (in the presence of 3.4 μM EDTA) electrolyte. The results were averaged to obtain the FE of CO. After the measurement, the working electrodes were tested via XPS to determine trace metal deposition and the upper limit active site density.

4. XPS trace metal deposition and LODs

XPS measurements to detect trace metal deposition were collected on thin film Au (as described in kinetics measurements) before and after electrolysis conditions. Electrolysis was performed in a CO_2 purged 0.1M $NaHCO_3$ with -1.2 V vs. Ag/AgCl. For XPS measurements corresponding to electrode deactivation, kinetics were run simultaneously to confirm Au deactivation. For purified samples that use EDTA, 3.4μM of EDTA was added to the electrolyte soltuion. XPS spectra were collected with a Kratos Axis Ultra X-ray photo-electron spectrometer (monochromatic Al Kα X-ray source, E_{photon} = 1486.6 eV, pass energy 20 eV). The binding energy scale was calibrated using the C 1s peak (BE = 284.5 eV) from typical surface contamination on the Au electrode. All peak areas were integrated using Casa XPS software and adjusted for atomic sensitivity accordingly.

High resolution spectra of the most common trace metal impurities reported in the literature (Zn, Cu, Fe, and Pb)[4–6] were collected on each sample. The Pt 4f region was also collected to evaluate Pt leaching onto the Au surface during electrocatalysis. Below in Figure S2 are the the high resolution spectra of Fe 2p, Pb 4f, and Pt 4f which are not included in the main text. The non-zero signal seen here for Pt 4f is due to the overlap of the Au $5p_{3/2}$ feature in this region, confirmed in our previous work.[7] The surface was also probed after 16 h of electrolysis and is given in Figure S3

The XPS LOD for each trace metal on a Au surface was calculated using the method outlined by Shard[8] for a homogeneously mixed trace element within a matrix element. The background signal of a clean (pre-electrolysis) Au electrode was collected within the binding energy ranges of each trace metal impuritites. These results can be see in the main text (for Cu and Zn) and below (for Fe and Pb).

The LOD for each possible trace element was calculated using Eq. 1 below:

$$X_{LOD}(a) = \frac{\sigma_B}{\sigma_B + \frac{\epsilon^{0.5} \cdot s_a}{\kappa} \sum \frac{A_i}{s_i}} \tag{1}$$

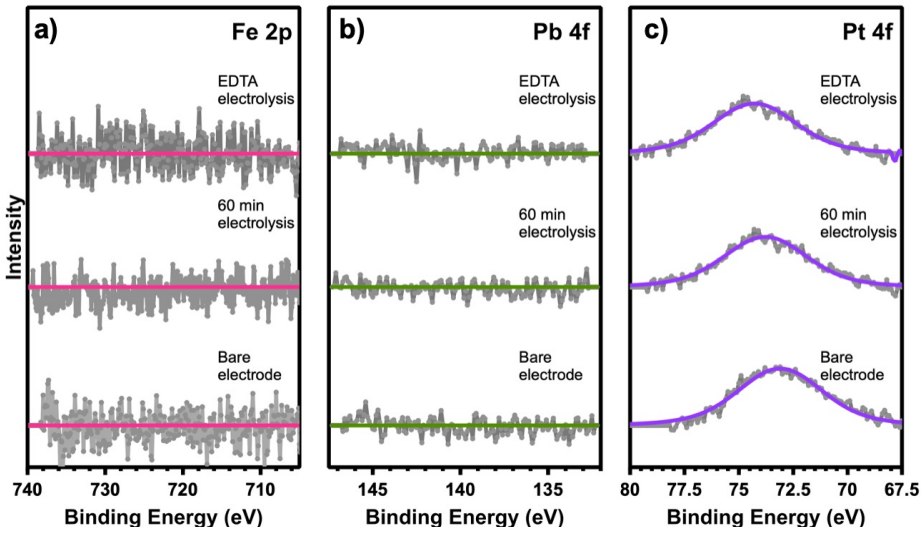

Figure S3: Au electrodes following various experimental conditions in the binding energy regions of a) Fe 2p b) Pb 4f and c) Pt 4f

where σ_B is the standard deviation of the background intensity in counts over the binding energy range of a particular trace metal. ϵ is the step size of the acquired data (0.1 eV used here). s_a and s_i are the relative sensitivity factors (RSF) of the trace metal and matrix element, respectively. κ, the detection limit scaling factor, is taken to be 9 $eV^{0.5}$. A_i is the area (in counts) of the Au 4f peak.

To account for the trace metals deposited on the Au surface opposed to homogeneously mixed throughout, the Au 4f area was adjusted by taking into account the surface-to-bulk intensity ratio of the XPS signal. The inelastic mean free path (λ) for Au was calculated to be 2.01 nm using Eq. 2,[9] giving a probe depth of 6.03 nm. The Au lattice spacing of a (111) surface (0.238 nm) was used to determine that approximately 26 layers of Au are probed during the XPS measurements.

$$\lambda = \frac{177}{E^2} - 0.054\sqrt{E} \tag{2}$$

The surface-to-bulk intensity ratio (calculated using Eq. 3) was determined to be about 11%. A_i in Eq. 1 was adjusted for this ratio to determine the LOD of certain trace metals deposited on top of the Au electrode. The final XPS LOD of impurities on the Au surface

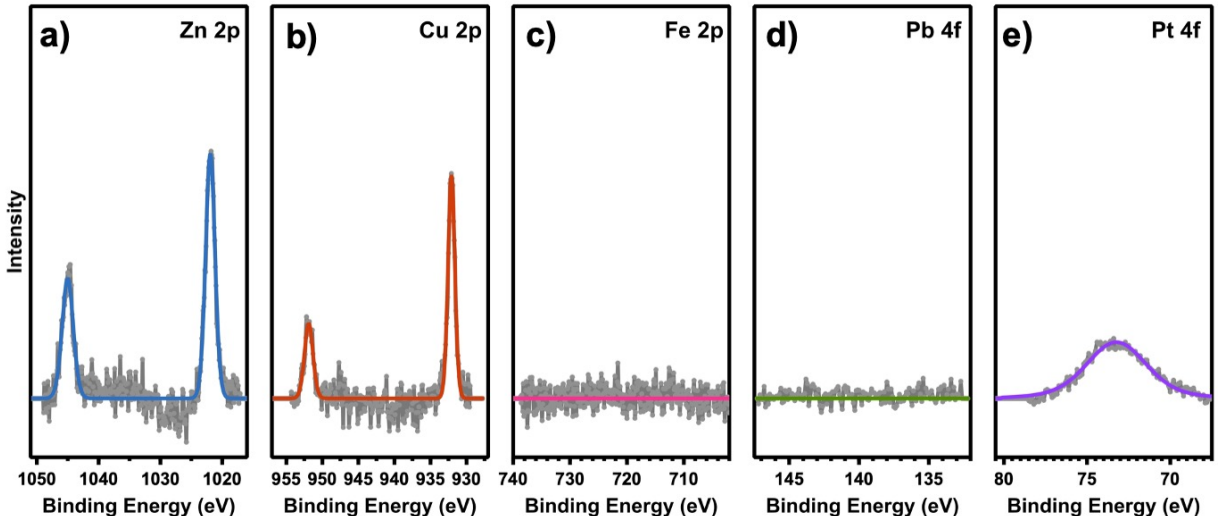

Figure S4: Au electrodes following 16 h under -1.2 V vs. Ag/AgCl bias in the binding energy regions of a) Zn 2p and b) Cu 2p c) Fe 2p d) Pb 4f and e) Pt 4f

are given in Table S1. These values represent the atomic LODs for the trace metals probed in this study. The high LOD for Pt is due to the interference of the Au 5p in this region. The feature leads to a large σ_B term in Eq. 1, raising the calculated LOD for Pt 4f.

$$\frac{Signal_{surf}}{Signal_{bulk}} = \frac{I_0(e^{\frac{-0}{\lambda}})}{I_0(e^{\frac{-0}{\lambda}} + e^{\frac{-0.238}{\lambda}} + e^{\frac{-0.476}{\lambda}} + e^{\frac{-0.714}{\lambda}} + ...)} \tag{3}$$

Table S1: Calculated XPS atomic LODs for trace metals on Au thin film

Orbital	Surface LOD
Zn 2p	0.49 %
Cu 2p	0.68 %
Fe 2p	0.45 %
Pb 4f	0.41 %
Pt 4f	2.6 %

5. CO spectra and Stark tuning slopes

The VSFG measurement taken under CO purging conditions were repeated a couple of times for each cation. The Stark tuning slopes shown in the manuscript and used for further calculations are the averaged result of these trials. Here we show one set of data for each of the cations except Rb^+, already shown in the manuscript.

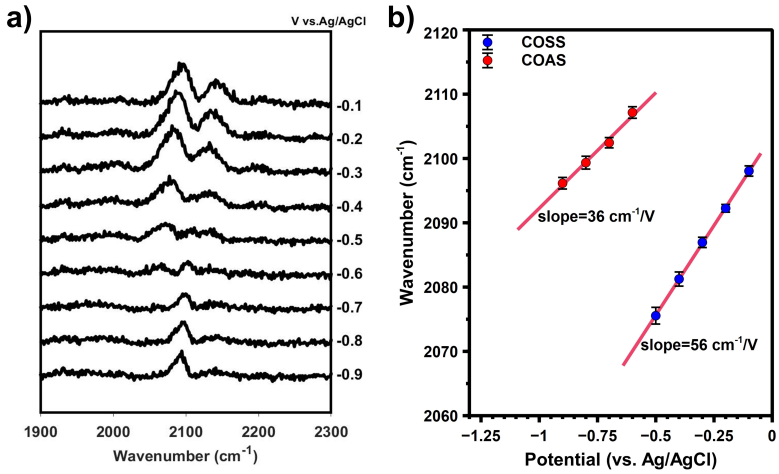

Figure S5: a) CO spectra obtained in $LiHCO_3$ which shows COSS at less negative potentials and COAS sites at more negative potentials; b) Potential-dependent frequency shift of CO adsorbed at two types of sites show different Stark tuning slopes.

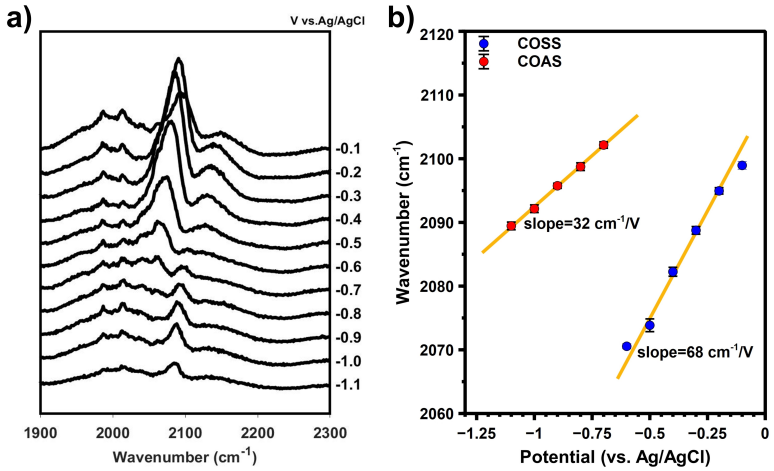

Figure S6: a) CO spectra obtained in $NaHCO_3$ which shows COSS at less negative potentials and COAS sites at more negative potentials; b) Potential-dependent frequency shift of CO adsorbed at two types of sites show different Stark tuning slopes.

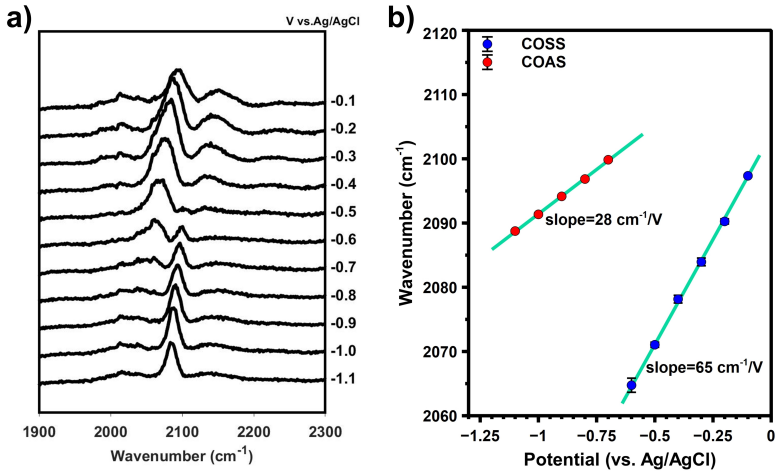

Figure S7: a) CO spectra obtained in $KHCO_3$ which shows COSS at less negative potentials and COAS sites at more negative potentials; b) Potential-dependent frequency shift of CO adsorbed at two types of sites show different Stark tuning slopes.

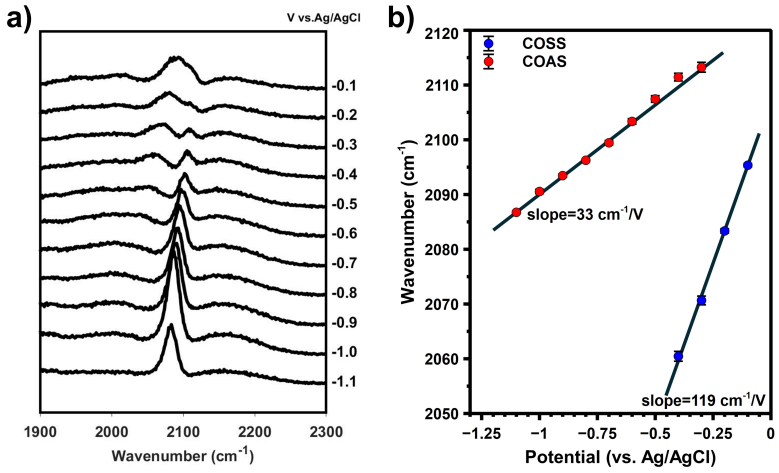

Figure S8: a) CO spectra obtained in $CsHCO_3$ which shows COSS at less negative potentials and COAS sites at more negative potentials; b) Potential-dependent frequency shift of CO adsorbed at two types of sites show different Stark tuning slopes.

6. Disentangling dipolar-coupling effects

The field-induced Stark effect, chemical shift effects, and coverage-induced dipolar-coupling effects could all potentially contribute to the observed frequency shift of adsorbed molecules. An applied potential will cause a variation of bonding between adsorbed molecules and the electrode and a field-dependent Stark shift, simultaneously. It is not trivial to fully resolve the contributions from each of these effects. However, it is possible to elucidate dipolar-coupling effects from the observed frequency shifts. In this section, we seek to disentangle the contribution from dipolar-coupling effects by treating the Stark effect and chemical shift as a whole, while as described in the manuscript and following Section 8, we calibrate the Stark tuning rate to address the chemical shift effect.

The frequency ($\omega(\phi, \Theta)$) can be expressed as a function of applied potential (ϕ) and coverage (Θ), as described by Eq. 4:[10]

$$\omega(\phi, \Theta) = K_\phi(\phi - \phi_0) + K_\Theta \Theta + \omega_0 \tag{4}$$

K_ϕ is the intrinsic Stark tuning slope, and K_Θ is the slope-constant associated with the adsorbate surface coverage. w_0 is the reference frequency at reference potential (ϕ_0). To derive the apparent Stark tuning slope (K_{app}), which was obtained from VSFG measurement for COSS, the total derivative in ϕ of Eq. 4 can be determined as:

$$K_{app} = \frac{d\omega(\phi, \Theta)}{d\phi} = \frac{\delta\omega}{\delta\phi} \cdot \frac{d\phi}{d\phi} + \frac{\delta\omega}{\delta\Theta} \cdot \frac{d\Theta}{d\phi} = K_\phi + K_\Theta \cdot \frac{d\Theta}{d\phi} \tag{5}$$

To disentangle the contribution of the dipolar-coupling term ($K_\Theta \cdot \frac{d\Theta}{d\phi}$) from the apparent Stark tuning slope, the potential-jump experiment, as previously described,[10] was first conducted to resolve K_Θ in 0.1 M $NaHCO_3$ under CO_2 purging. A series of potential steps were first applied to the Au electrode (-0.1 V to -0.9 V vs. Ag/AgCl, holding for 1 min at each potential), consistent with VSFG measurements. The bias was switched and held

at -0.3 V vs. Ag/AgCl, where COSS adsorption is usually at a maximum. VSFG spectra were continuously collected with 5 s integration for each spectra (Figure S9a) The COSS intensity increases significantly in the first 20 s and then stabilizes, indicating the CO reaches a saturated coverage, while the frequency blue-shifts in the same time period as the COSS intensity increase before stabilizing (Figure S9b). Since the applied potential remained consistent throughout this time period, the blue-shift is solely induced by the dipolar-coupling effect resulting from the increase in COSS coverage on the Au surface. A simple way to explain the observed blue-shift is that the external field induced by the parallel dipole field from neighboring adsorbed CO could accelerate the vibrational frequency, although a more complete explanation can be derived by introducing a mutual energy term into the system's total energy expression.[11,12] VSFG intensity is quadratically correlated with the adsorbate's number density,[13] thus, the relative coverage of adsorbed CO was calculated by the square root of the COSS signal intensity normalized to the square root of the VSFG intensity after the frequency (and coverage) stabilization. A linear relationship between the frequency and relative coverage is then obtained (Figure S9c) with a slope of K_Θ.

We then calculate the potential-dependent relative coverage of COSS for each cation used here (Figure S9d), and fit with a linear function to obtain $\frac{d\Theta}{d\phi}$, as given in the first row of Table S2. The dipolar-coupling term ($K_\Theta \cdot \frac{d\Theta}{d\phi}$) is then calculated, and subtracted from the apparent Stark tuning slope (K_{app}) to get the intrinsic Stark tuning slope (K_ϕ) (Table S2) for each cation. The dipolar-coupling term is about 10% of K_{app}, indicating the dipole-dipole coupling effect caused by CO coverage change is not dominating the observed frequency shift. The cation dependent trend for the intrinsic Stark tuning slopes still increases from Li^+ to Cs^+, which further confirms that the Stern layer thickness decreases for larger alkali cation.

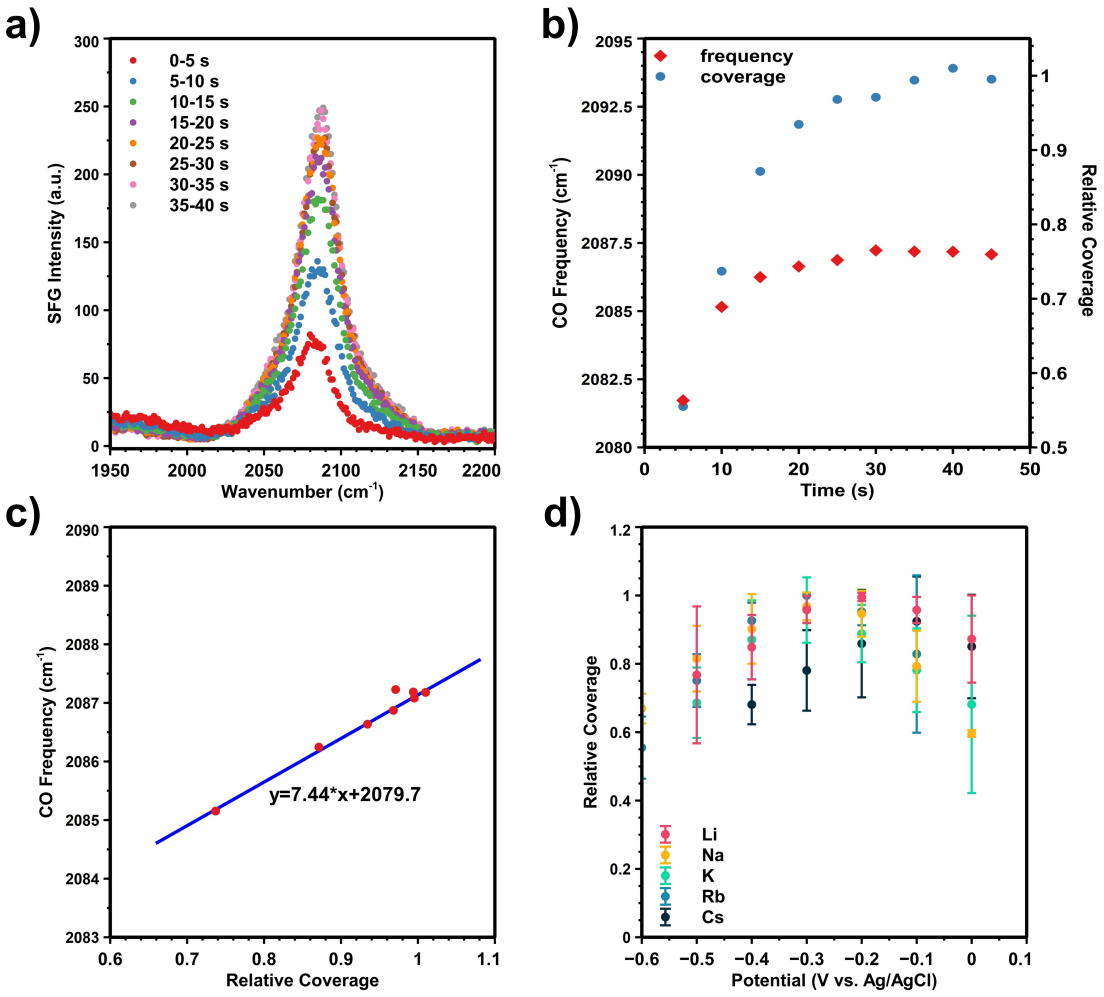

Figure S9: a) Time-dependent CO spectra obtained at -0.3 V vs. Ag/AgCl following a potential jump from -0.9 V; b) COSS frequency shift and relative coverage change versus time; c) The linear relationship between the CO frequency shift and relative coverage; d) Potential-dependent CO coverage change for each cation. The intensity of COSS peak was normalized to the intensity at CO maximum adsorption potential, and taken the square root to calculate the relative coverage. The relative coverage is assume to be 1 at maximum absorption potential. The error bar results from averaging multiple trials conducted for each cation.

Table S2: Derived dipolar-coupling terms, K_{app}, and K_{ϕ} for different cations

	Li^+	Na^+	K^+	Rb^+	Cs^+
$\frac{d\Theta}{d\phi}$ (V^{-1})	0.8 ± 0.1	1.0 ± 0.1	1.4 ± 0.3	1.5 ± 0.2	0.8 ± 0.1
$K_{\Theta} * \frac{d\Theta}{d\phi}$ (cm^{-1}/V)	5.9 ± 0.7	7.3 ± 0.7	10.1 ± 2.2	11.2 ± 1.5	6.0 ± 0.7
K_{app} (cm^{-1}/V)	66.2 ± 2.9	70.5 ± 1.8	75.2 ± 5.7	85.5 ± 3.4	103.8 ± 5.1
K_{ϕ} (cm^{-1}/V)	60.3 ± 3.6	63.2 ± 2.5	65.1 ± 7.9	74.3 ± 4.9	97.8 ± 5.8

7. Potential of zero charge measurement

To measure the potential of zero charge (PZC) for CO saturated $MHCO_3$ electrolytes, electrochemical impedance (EIS) measurements were taken at potentials in the range of 0.2 V to -0.4 V vs. Ag/AgCl over a frequency range from 200 kHz to 100 mHz. The electrolytes were diluted to 1 mM to determine the PZC accurately by the EIS method.[14] The double layer capacitance was calculated by fitting the EIS data with an equivalent circuit as suggested by Xie et al.[15] using Zview software. The extrapolated potential of the minimum double layer capacitance was taken as the PZC, which are -0.30 V, -0.25 V, -0.25 V, -0.30 V, and -0.15 V for Li^+ to Cs^+, respectively.

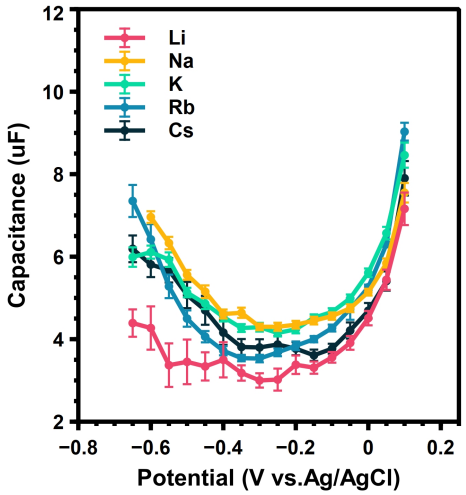

Figure S10: Double layer capacitance data obtained from fits of electrochemical impedance data for alkali cations. Error bars represent the standard deviation of multiple measurement.

8. Stark tuning slopes and Stern layer thicknesses

The Stern layer thicknesses are derived from the Stark tuning data and measured PZC using the Gouy-Chapman-Stern (GCS) model, as described previously.[7] More specifically, assuming the value (3.5 Å) for the OHP of Cs^+, we calibrate the Stark tuning rate for COAS and COSS, i.e. 1.40 $cm^{-1}/(MV/cm)$ and 4.29 $cm^{-1}/(MV/cm)$, respectively. Then the Stern layer thicknesses are derived from the intrinsic Stark tuning data after excluding dipolar-coupling effect for COSS. Table S3 shows the intrinsic Stark tuning slopes and derived Stern layer thicknesses for COSS and COAS from the procedure outlined here. The experimentally obtained apparent Stark tuning slopes and the process of calibrating dipolar-coupling effect is already shown in Table S2.

Table S3: Stark tuning slopes (k) and calculated Stern layer thicknesses (d_S) at spectator vs. active sites

	COSS		COAS	
Cation	k(cm^{-1}/V)	d_S(Å)	k(cm^{-1}/V)	d_S(Å)
Li^+	60.3 ± 3.6	6.7 ± 0.2	35.5 ± 0.8	3.4 ± 0.2
Na^+	63.2 ± 2.5	6.3 ± 0.2	32.2 ± 0.3	3.8 ± 0.1
K^+	65.1 ± 7.9	5.4 ± 0.7	31.5 ± 0.6	3.9 ± 0.1
Rb^+	74.3 ± 4.9	4.1 ± 0.4	29.2 ± 0.7	4.0 ± 0.1
Cs^+	97.8 ± 5.8	3.5	34.6 ± 1.6	3.5

References

(1) Wallentine, S.; Bandaranayake, S.; Biswas, S.; Baker, L. R. *J. Phys. Chem. A* **2020**, *124*, 8057–8064.

(2) Wallentine, S.; Bandaranayake, S.; Biswas, S.; Baker, L. R. *J. Phys. Chem. Lett.* **2020**, *11*, 8307–8313.

(3) Shang, H.; Wallentine, S. K.; Hofmann, D. M.; Zhu, Q.; Murphy, C. J.; Baker, L. R. *Chem. Sci.* **2020**, *11*, 12298–12306.

(4) Wuttig, A.; Surendranath, Y. *ACS Catal.* **2015**, *5*, 4479–4484.

(5) Hori, Y.; Konishi, H.; Futamura, T.; Murata, A.; Koga, O.; Sakurai, H.; Oguma, K. *Electrochim. Acta* **2005**, *50*, 5354–5369.

(6) Hori, Y. i. *Modern aspects of electrochemistry*; Springer, 2008; pp 89–189.

(7) Zhu, Q.; Wallentine, S. K.; Deng, G.-H.; Rebstock, J. A.; Baker, L. R. *JACS Au* **2022**, *2*, 472–482.

(8) Shard, A. G. *Surf. Interface Anal.* **2014**, *46*, 175–185.

(9) Seah, M. P.; Dench, W. *Surf. Interface Anal.* **1979**, *1*, 2–11.

(10) Pfisterer, J. H.; Zhumaev, U. E.; Cheuquepan, W.; Feliu, J. M.; Domke, K. F. *J. Chem. Phys.* **2019**, *150*, 041709.

(11) Hollins, P.; Pritchard, J. *Prog. Surf. Sci.* **1985**, *19*, 275–349.

(12) Severson, M. W.; Stuhlmann, C.; Villegas, I.; Weaver, M. J. *J. Chem. Phys.* **1995**, *103*, 9832–9843.

(13) Lagutchev, A.; Lu, G.; Takeshita, T.; Dlott, D. D.; Wieckowski, A. Vibrational sum frequency generation studies of phase transition of CO on Pt (111) and Pt (111)/Ru electrodes. 233rd ACS National Meeting. 2007.

(14) Ojha, K.; Arulmozhi, N.; Aranzales, D.; Koper, M. T. *Angew. Chem.* **2020**, *132*, 721–725.

(15) Xie, X.-H.; Li, E. L.; Tang, Z. K. *Int. J. Electrochem. Sci.* **2010**, *5*, 1018–1025.